LAWRENCE
LIVERMORE
NATIONAL
LABORATORY

LLNL-JRNL-647475

Electron Beam Weldability of a Group IAB Iron Meteorite

J. W. Elmer, C. L. Evans, J. J. Embree, G. F. Gallegos, L. T. Summers

December 9, 2013

Science and Technology of Welding and Joining

Disclaimer

This document was prepared as an account of work sponsored by an agency of the United States government. Neither the United States government nor Lawrence Livermore National Security, LLC, nor any of their employees makes any warranty, expressed or implied, or assumes any legal liability or responsibility for the accuracy, completeness, or usefulness of any information, apparatus, product, or process disclosed, or represents that its use would not infringe privately owned rights. Reference herein to any specific commercial product, process, or service by trade name, trademark, manufacturer, or otherwise does not necessarily constitute or imply its endorsement, recommendation, or favoring by the United States government or Lawrence Livermore National Security, LLC. The views and opinions of authors expressed herein do not necessarily state or reflect those of the United States government or Lawrence Livermore National Security, LLC, and shall not be used for advertising or product endorsement purposes.

Electron Beam Weldability of a Group IAB Iron Meteorite

By:

J. W. Elmer*, C. L. Evans*, J. J. Embree*, G. F. Gallegos*, and L. T. Summers*

*Materials Engineering Division, Lawrence Livermore National Laboratory, Livermore, CA, USA

Abstract

Electron beam welding, first demonstrated in space on Soyuz 6, and later on the Skylab mission, appears to be the leading candidate for welding structures in space since it is ideally suited for the vacuum of space. These pioneering space welding experiments were performed on terrestrial materials such as aluminum, titanium and stainless steel, and the results showed no significant differences from welds made on Earth. Future weld construction of large scale space structures, however, will need to exploit natural space resources for raw materials, and iron is expected to be a key element due to its availability in near-Earth objects. Here, we investigate the weldability of an extraterrestrial group IAB iron meteorite in its native state, and show that further welding innovation is required to directly join meteoritic material due to inherent non-metallic impurities that lead to weld cracking.

Introduction

Commercial space activities are now beginning in earnest with SpaceX's recent successful berthing to the International Space Station, and the recent incorporation of Planetary Resources, an asteroid-mining company[1]. These private ventures open up new possibilities for space exploration, including scientific as well as economic pursuits, and lead the way for potential space manufacturing and future colonization[2]. Colonies and/or space manufacturing facilities will only be feasible if they rely minimally on material exports from Earth due to the high cost penalty of transportation through Earth's gravitational field. Rather, bulk materials for space construction are likely to come from the Moon, near-Earth objects, or asteroids, which are known to be rich in mineral and metal content[3]. Metals have favorable structural properties, and iron, which is the most abundant metallic element in our galaxy[4], makes it a likely candidate for space construction. Iron is known to exist in its metallic form in iron meteorites, however, it is unknown if the types of welding experiments performed on terrestrial materials in space[5] will be able to be used to directly join iron from extraterrestrial sources.

The Canyon Diablo meteorite, responsible for the 1.3 km diameter Meteor Crater in Arizona, is a group IAB iron meteorite containing approximately 90% Fe, 7.2% Ni, 0.5-1% C, 0.5-1%S, 0.46% Co, and 0.26% P by weight, with silicates and other minor elements also present[6]. The meteor is speculated to have been 25m in diameter and to have weighed approximately 63,000 tons[6]. This mass is equivalent to eight times the total amount of iron contained in the Eiffel tower, and was originally pursued as a commercial source of iron. The meteor is classified as a coarse octahedrite, Og, with a microstructure composed mainly of kamacite, which is an Fe-Ni alloy having the same body centered cubic, bcc, crystal structure as iron and low carbon steels[6]. The microstructure also contains a few percent of taenite, a nickel rich Fe-Ni alloy having the same face centered cubic, fcc, crystal structure as austenitic stainless steels[7]. The remainder of the microstructure contains up to 10% iron and nickel carbides, sulfides and phosphides, as well as silicates, graphite, and diamond[6,7]. It is estimated that 30 tons of the Canyon Diablo meteor have been collected[6], making it readily available for scientific studies, and the large metal fraction in this meteorite makes it an ideal candidate for welding studies.

Results and Discussion

The meteorite fragment used for these studies is shown in Figure 1a and is a 722.6g Canyon Diablo specimen that was acquired for this investigation[8]. The fragment measured approximately 5x6x9 cm, and is covered with a dark colored oxidized fusion crust. Figure 1b shows a photograph of a 6 mm thick section removed from the meteorite, which has been polished in preparation for welding. The cross section displays cracks near its edges, which allowed terrestrial oxidation to occur along the visible crack veins.

The major phases that exist in meteorites have a close parallel to those that form in Fe-Ni alloys, but the nomenclature is different, drawing heavily on mineralogy for description of the phases. Table 1 summarizes the compositions, crystal structures and typical morphologies[9-12] of the major phases in the meteorite, and compares them with similar phases in steel and cast iron. Metallographic characterization of the microstructure was performed on samples polished using colloidal silica prior to welding. The major phases that were identified are shown in Fig. 2 based on their morphological characteristics[3,6,7,9]. Figure 2a shows a field of view that is typical of the majority of the meteorite microstructure. Prismatic and platelet rhabdites $(FeNiCo)_3P$ occur throughout the kamecite. Rhabdites are believed to nucleate homogeneously from kamecite[12], and are distributed with sub-millimeter spacing in the majority of the surface examined. Neumann bands, shock induced mechanical twins, are also present and are known to form parallel to the (112) planes of kamecite[6]. Figure 2b shows a large and fractured cohenite nodule $(FeNiCo)_3C$, light color, with graphite, black, and other included phases. The cohenite nodules are not evenly distributed in the microstructure, and

are spaced at greater than one centimeter distances from each other. Figure 2c shows a light colored taenite particle with kamecite nucleated throughout its interior in the center of the micrograph. Several schreibersite particles $(FeNiCo)_3P$, which are compositionally similar to rhabdite, are also present. Figure 2d shows a dark colored complex inclusion situated next to the vertical plessite wedge (taenite mixed with fine nucleated kamecite) after lightly etching in a 2% nitric acid and alcohol solution. Troilite (FeS) was not clearly identified in the cross section to be welded, but is known to be a phase that exists in the Canyon Diablo meteorite at approximately 1% by volume[7].

Electron beam welding was performed on this specimen at Lawrence Livermore National Laboratory using a high voltage machine (Hamilton Standard, SN 605) operating at $5x10^{-5}$ Torr vacuum. The electron beam power was fixed at 1.0kW (10mA at 100kV), and welds were made at two different travel speeds of 17 and 68 mm/s. The electron beam was sharp focused on the surface of the sample, and had a Gaussian-shaped power density distribution with a peak power density of 13.1kW/mm^2, a beam diameter of 0.42 mm, and a full width half maximum dimension of 0.24 mm as measured by the Enhanced Modified Faraday Cup diagnostic[13]. Post weld observations show variations in the surface roughness due to weld eruptions, craters, and spatter, while the weld surface varied in color from light grey to nearly black in places. The two different weld parameters were selected so as to produce partial penetration melt depths (2 mm and 5mm deep) in the 6 mm thick meteorite slice. Each weld solidified with a different cooling rate, which was estimated to be on the order of 10^3 and 10^4 °C/s for the slow and fast speeds respectively, based on similar electron beam welds made previously on stainless steel alloys[14]. These weld cooling rates are 10^{14}-10^{15} times faster than the original cooling rate of meteorites, which are estimated to cool at rates on the order of 100°C per million years[3].

The microstructure of these welds is expected to be considerably different than that of the native meteorite due to the effects of cooling rate on solidification and subsequent solid state phase transformations as the weld cools to room temperature. The initial microstructure of the meteorite is large grained, and one of nearly single crystal kamecite relative to the size of the welds[3]. Epitaxial regrowth of a weld from single crystal base metal constrains the solidification microstructure to certain crystallographic orientations, producing textured weld microstructures[15]. At high cooling rates, solidification features creating this texture, such as cells and dendrites, are known to reduce in size and also contain composition gradients due to insufficient time for diffusional homogenization[14]. Solid state transformation of the high temperature taenite phase to the low temperature kamecite phase will be affected by these composition gradients, and also by the reduced time for redistribution of alloying elements such as Ni, Co, and C. These effects can alter the taenite transformation mechanism from diffusional controlled, that produces a Widmanstätten microstructure, to partitionless, that produces a martensitic transformation microstructure, at high cooling rates[16].

The effects of solidification on the weld microstructure can be predicted with the aid of computational thermodynamics. Here we use Thermocalc 3.0.1 with the TCFE3 database and the Scheil model to calculate the phases that form during weld solidification[17]. These calculations were performed with cohenite as the carbide phase, excluding graphite and diamond that are not expected to form during the fast cooling rate of welds. The bulk composition of the Canyon Diablo meteorite is an input to the solidification model, and has been measured on many occasions with some variability depending on the relative amounts of the different phases that are incorporated in the sample being analyzed[18]. Table 2 summarizes the composition of the meteorite fragment used in this study, where X-ray fluorescence was performed on the bulk meteorite fragment (Thermo Scientific Niton XL3t XRF Analyzer at 70 kV) to determine its major metallic elements. The non-metallic elements, S and C, were measured using LECO combustion analysis, while P was measured using absorption spectroscopy on small samples weighing 1-2 gram each. The XRF results show the metallic composition to be 7.6 wt% Ni, 0.49 wt% Co, and remainder Fe. The Ni content is slightly higher than the average reported value of 7.2 wt% Ni[6], but is within the accepted range[18], while the Co content is nearly identical to the reported average value of 0.46 wt%[6,18]. The measured S and C contents can only be considered to be approximate since these elements are distributed heterogeneously in the microstructure on a scale larger than the sample examined. Here we measured S at less than 0.005 wt%, and carbon at 0.30± 0.18 wt% based on four samples. The P content was measured at 0.19 wt% and is likely to be representative of the content in the meteorite sample due to the finer distribution of phosphides than the carbides or sulfides.

Thermodynamic calculations of solidification were performed using the measured composition of 7.6 wt% Ni, 0.30 wt% C, 0.49wt% Co, 0.19 wt% P, and 0.005 wt% S with the remainder Fe. Using the Scheil model, Figure 3 plots the fraction solid phase versus temperature during the final stages of solidification. Liquid, L, initially solidifies as taenite, T, starting at a temperature of 1426°C. No new solid phases appear until the temperature has dropped to 1075°C, where taenite makes up 97.1% of the microstructure with the remainder being liquid. The composition of the taenite and liquid were calculated at this point, showing that phosphorous (0.39 wt%) and sulfur (0.20 wt%) have partitioned to the liquid where they act as melting point suppressants. During cooling below 1075°C, the $(FeNiCo)_3C$ carbide phase, C', appears with liquid and taenite. At 1052°C, the $(FeNiCo)_3P$ phosphide phase, P', appears with the other phases. Finally, at 1049°C the FeS sufide phase, S', appears prior to final solidification that occurs at 1048°C as the remaining liquid solidifies to a mixture of phases. Note that the final solidification temperature is 378°C below the point where taenite first began to solidify, representing a very large liquid+solid solidification temperature range.

A photograph of a polished cross section of the electron beam weld made at 68 mm/s is shown in Fig. 4a. This weld is 2.0 mm deep, and has a combined fusion zone (FZ) plus heat affected

zone (HAZ) width of approximately 1 mm. Rhabdites and Neumann bands are visible in the base metal, distinguishing it from the coarser textured HAZ, while distinction between the HAZ and FZ is not clear in this weld. The fusion zone, is approximately 0.6 mm wide and has a keyhole shape being deeper than it is wide, with visible centerline and branching cracks. Fig. 4b shows higher magnification of a cracked region. This sample was lightly etched in a solution of 2% nitric acid and alcohol to reveal the grain boundaries and cells within the grains of the largely ferritic microstructure. The solidification-formed cells are spaced approximately 6 μm apart, which indicates a cooing rate of approximately 10^3-10^4 °C/s[14]. A grain boundary film is seen along many of the cracked and uncracked grain boundaries, and small dark-etching particles appear in the cell boundaries. The morphology of the cracks suggests that they initiated while the metal was solidifying, and are commonly referred to as weld solidification cracks[19]. Such cracks are known to occur in steel alloys with high phosphorous and sulfur, since these elements partition to the remaining liquid during solidification, creating weak grain boundaries that can be pulled apart by the welding induced strains as the weld cools[19]. This theory is consistent with the results of the Scheil solidification calculation shown in Fig. 3, which predicted a large solidification temperature range and associated partitioning of phosphorous and sulfur at the final stage of solidification.

To further investigate the solidification cracking mechanism, scanning electron microscopy (SEM) was performed to map elemental partitioning near the tip of one of the FZ cracks using a JEOL-8200 electron microprobe. The backscattered electron and x-ray maps were acquired at 15 kv accelerating voltage, and X-ray maps were acquired using both energy dispersive (EDS) and wavelength dispersive spectroscopy (WDS). A focused beam was used with beam currents between 2 and 50 na for EDS and WDS analysis respectively. Fig. 5a shows the SEM backscattered image near a crack tip (upper left) in the 68 mm/s weld. When imaged for phosphorous, Fig. 5b indicates that the phosphorous is heavily concentrated in veins emanating from the crack tip region. Phosphorous is also enriched in the many small precipitates that are present throughout the microstructure. Other results show that the veins are enriched in Fe and Ni, but do not contain substantial amounts of sulfur or carbon, thus they would likely be similar in composition to rhabdites or schreibersite, $(FeNiCo)_3P$. These results confirm the weld solidification cracking mechanism, whereby the well distributed rhabdites and schreibersite particles in the kamecite base metal are incorporated into the liquid weld pool, and then concentrate at the cell and grain boundaries during the final stages of solidification.

Microhardness measurements were made in the base metal, FZ, and HAZ of both welds using a Vicker's microhardness method with a 50g load. The average hardness for each region is reported in Table 3, along with the standard deviation based on a minimum of 10 samples for each reading. The results show that the base metal kamecite has a hardness of approximately 190 HV, which indicates minimal shock hardening of this specimen[7]. The HAZ of both welds

showed nearly the same hardness as the base metal and cannot be statistically distinguished from the base metal or from each other. The high cooling rate in the HAZ of the weld would suggest that the transformation from taenite to kamecite would occur by a martensitic mechanism[17], which is known to harden high carbon steels considerably relative to the base metal[19]. However, since there is no change in hardness between the base metal and HAZ, one can conclude that the kamecite is nearly a pure iron-nickel alloy with very low carbon so as not to produce a martensitic hardening effect. The low carbon content of the kamecite is consistent with its slow cooling rate extraterrestrial past whereby the carbon has nearly all segregated to the cohenite and graphite phases on a spatial distribution scale that is large compared to the weld HAZ.

Unlike the HAZ, the weld FZ was shown to be harder than the base metal. Table 2 indicates that the weld made at 68 mm/s had an average FZ hardness of 236 HV, while the weld FZ made at 17 mm/s was significantly harder at 408 HV. As in the case of the 68 mm/s weld, solidification cracks are present along the weld centerline of the 17 mm/s weld, as indicated in Fig. 6a. This figure further shows the hardness indentations made across the weld at its mid-depth location. Figure 6b plots the microhardness results across the weld fusion zone, where it is clear that the hardness rapidly increases in the FZ to approximately twice its HAZ value, and that the HAZ and base metal have the same hardness as each other. It is speculated that the high hardness of the weld FZ is a result of the incorporation of carbon from cohenite or graphite particles into the liquid weld pool. When combined with the high cooling rate of the welds, the increased carbon content of the FZ allows martensite to form during the solid state transformation of taenite on cooling. This level of hardness, 408 HV, would be similar to a steel containing 0.2% carbon that has been quenched to form martensite[20].

The microstructure of the 17 mm/s weld is shown in Fig. 7a in the etched condition near the fusion line. Solidification cracks are present near the centerline of the weld and martensite is present in the fusion zone of this weld, confirming the hardening mechanism revealed by the microhardness traverse. Figure 7b shows a different portion of this weld where the light etching cohenite band on the left side of the weld has partially dissolved into the FZ, creating plate type martensite. The cohenite particles are very hard, and were measured here to be 1155± 58.3 HV. The martensite close to the cohenite particle had hardness values that varied from 450 to 540 HV presumably due to increased carbon concentrations near the coehnite particle. Because of the inhomogeneous distribution of the high-carbon cohenite particles in the starting microstructure, the fusion zone hardness is likely to vary from weld to weld, and also vary along the length of a given weld, depending upon the random incorporation of cohenite or graphite into the liquid weld pool prior to solidification. Locations of high carbon content will have high hardness and associated low ductility, creating a second potential source of weld cracking that may be difficult to predict.

Summary and Conclusions

Electron beam welds made on a group IAB iron meteorite illustrate some of the welding challenges that will be faced if future efforts are required to join structural meteoritic iron components in their native state. In the case of the Canyon Diablo meteorite, we show that its high phosphorous content, which is distributed on a sub-millimeter scale throughout the majority of the microstructure in the form of $(FeNiCo)_3P$ rhabdite and shcreibersite particles, leads to solidification cracking during the high inherent cooling rate of electron beam welds. Sulfur, if present as troilite, would be expected to produce similar results, and the consequential centerline and grain boundary solidification cracks would be detrimental to the strength of the weld join as well. The high carbon content of this meteorite presents further weldability concerns. Carbon containing particles in the form of $(FeNiCo)_3C$ cohenite, or graphite, tend to be larger and more heterogeneously distributed than the phosphides, having spacing of a centimeter or more. Here we show that the chance incorporation of these particles into the weld creates increased, and variable, weld hardness, which is an additional fusion zone cracking concern. Based on our observations, we conclude that the weldability of iron meteorites is dominated by the amount and distribution of carbon, phosphorous, and sulfur containing phases in the starting meteorite microstructure. Innovative welding approaches will be required to create sound welds in meteorites, including the development of suitable filler metals that will modify the fusion zone composition to better incorporate and control the inherent non-metallic elements found in iron meteorites.

Acknowledgments

The authors would like to thank LLNL coworkers G. R. Gibbs for performing the electron beam welds, R. J. Ryerson for SEM/EDS, J. A. Rodrigues for x-ray florescence, and R. R. Thompson for radiography of the as received meteorite. This work was performed under the auspices of the U.S. Department of Energy by Lawrence Livermore National Laboratory under Contract DE-AC52-07NA27344.

References

1. Elvis, M., Let's mine asteroids- for science and profit. *Nature*, **485**, Issue 7400, 549, May 31, 2012.
2. Eckart, P. *LSC The Lunar Base Handbook: An Introduction to Lunar Base Design.* Learning Solutions 2nd Edition, 2006.

3. Buchwald, V. F. *Handbook of Iron Meteorites, Their History, Distribution, Composition and Structure, Vol. 1, Iron Meteorites in General*, University of California Press, 1975.
4. Croswell, K. *Alchemy of the Heavens.* Anchor, 1st edition, 1996.
5. *Space Technologies, Materials, Structures*, Edited by B. E. Paton, Taylor and Francis Inc., New York, 2003.
6. Buchwald, V. F. *Handbook of Iron Meteorites, Their History, Distribution, Composition and Structure, Vol. 2, Iron Meteorites, Abakan-Mejillones,* University of California Press, 1975.
7. Vdovykin, G. The Canyon Diablo Meteorite. *Space Science Reviews*, **14**, 758-831, 1973.
8. Aerolite Meteorites, LLC, Tucson, AZ, USA.
9. Heymann, D., Lipschutz, M. E., Nielsen, B., and Anders, E. Canyon Diablo Meteorite: Metallographic and Mass Spectrometric Study of 56 Fragments. *J. Geophysical Research*, **71**, 619-641, 1966.
10. Goldberg, E., Uchiyama, A., and Brown, H. The distribution of nickel, cobalt, palladium, and gold in iron meteorites. *Geochimica et Cosmochemica Acta*, **2**, 1-25, 1951.
11. Short, J. M., and Andersen, C. A. Electron Microprobe Analysis of the Widmanstätten Structure of Nine Iron Meteorites. *J. Geophysical Research*, **70(15),** 3745-3759, 1965.
12. Geist, V., Wagner, G., Nolze, G., Moretzki, O. Investigations of the meteoritic mineral $(Fe,Ni)_3P$. *Crys. Res. Technol.*, **40(1/2)**, 52-64, 2005.
13. Elmer, J. W., and Teruya, A. T. An Enhanced Faraday Cup for the Rapid Determination of the Power Density Distribution in Electron Beams. *Welding Journal*, **80**, 288s-295s, 2001.
14. Elmer, J. W., Allen, S. M., Eagar, T. W. Microstructural Development During Solidification Of Stainless Steel Alloys. *Metall. Trans. A*, **20A**, 2117-2131, 1989.
15. David, S. A., Babu, S. S., and Vitek, J. M., Welding: Solidification and Microstructure. *Journal of Metals*, **55(6)**, 14-20, 2003.
16. Yang, J. and Goldstein, J. I. The formation of the Widmanstätten structure in meteorites. *Meteorics and Planetery Science*, **40**, 239-253, 2005.
17. Andersson J.O., Helander T., Höglund L., Shi P.F., and Sundman B. Thermo-Calc and DICTRA, Computational tools for materials science. *Calphad*, **26**, 273-312, 2002.
18. Moore, C. B., Birrell, P. J., and Lewis, C. F. Variations in the chemical and mineralogical composition of rim and plains specimens of the Cañon Diablo meteorite. *Geochimica et Cosmochemica Acta*, **31**, 1885-1892, 1967.
19. Kou, S. *Welding Metallurgy*, Wiley Interscience 2nd Edition, 2002.
20. Grange, R. A., Hribal C. R., and Porter, L. F. Hardness of Tempered Martensite in Carbon and Low-Alloy Steels. *Metallurgical Transactions A*, **8A**, 1775-1785, 1977.

Table 1: Summary of major meteoritic phases observed in the Canyon Diablo meteorite, and similarities to conventional steel or cast iron alloys.

Meteorite				Similar steel or cast iron phase
Phase, constituent, or structure	Composition	Crystal Structure	Morphology	
kamacite	Fe-(Ni,Co), Ni~7%	bcc	large grained matrix phase	α-Fe, ferrite
Neumann bands	Fe-(Ni,Co), Ni~7%	bcc	shock induced twins in kamecite	twinned α-Fe, ferrite
taenite	Fe-(Ni,Co), Ni~30%	fcc	bands or wedge like features in kamecite	γ-Fe, austenite
Widmanstätten	Fe-(Ni,Co)	fcc+bcc	octahedral crystallographic pattern of taenite bands in kamecite	α-Fe + γ-Fe
plessite	Fe-(Ni,Co)	fcc+bcc	taenite bands or wedges with internally nucleated kamecite	α-Fe + γ-Fe
cohenite	$(Fe,Ni,Co)_3C$	orthorhombic	irregular shaped particles or large nodular shaped inclusions	cementite (Fe_3C)
graphite	C	hexagonal	nodular shaped inclusions, often found with cohenite	graphite nodules in cast iron
schreibersite	$(Fe,Ni,Co)_3P$	tetragonal	irregular particles heterogeneously nucleated near grain or interphase boundaries	Fe_3P exists in steel, but in very small amounts
rhabdite	$(Fe,Ni,Co)_3P$	tetragonal	homogeneously nucleated prismatic or plate shaped particles in kamecite	
troilite	(FeS)	hexagonal	nodular shaped inclusions	MnS, rather than FeS, forms in most steels

Table 2: Measured chemical composition of the meteorite fragment in wt%. Carbon was measured on 4 samples and one standard deviation is reported.

Fe	Ni	Co	P	S	C
Bal	7.6	0.49	0.19	<0.005	0.30±0.18

Table 3: Summary of the microhardness measurements for the meteorite base metal, fusion zone and heat affected zone of the two welds.

Weld Speed	Kamecite Base Metal	Weld HAZ	Weld FZ
(mm/s)	(HV)	(HV)	(HV)
68	192±10.7	190±10.5	236±11.9
17	187±9.7	188±12.6	408±35.8

Figure Captions

Figure 1: (a) Photograph of the as received meteorite on 1 cm square grids. (b) Photograph of the polished 6 mm thick by 62 mm wide section removed from the meteorite in preparation for electron beam welding.

Figure 2: Microstructural features of the as received meteorite: a) prismatic and plated shaped rhabdites with Neumann bands in a kamecite matrix, b) large fractured cohenite particle with graphite and other included phases. c) taenite particle with internal nucleated kamecite, surrounded by several schreibersite particles, d) unidentified inclusion adjacent to a wedge of fine grained plessite.

Figure 3: Scheil calculation of the final stages of weld solidification showing the successive phases that form as the remaining liquid becomes enriched in phosphorous and sulfur. L-liquid, T-FeNiCo (fcc taenite), C'-$(FeNiCo)_3C$, P'- $(FeNiCo)_3P$, S'-FeS. Compositions of the liquid and taenite phases are given just prior to the formation of the carbide phase.

Figure 4: (a) Weld made at 68 mm/s measuring 2.0 mm deep with a total heat affected zone width of approximately 1 mm. Centerline and grain boundary cracks are visible in the fusion zone, while rhabdites are visible in the kamecite base metal. (b) High magnification image of cracked region near the centerline of the 17 mm/s weld, showing grain boundary films and intercellular particles (lightly etched).

Figure 5: (a) Backscattered SEM image near the tip of a fusion zone crack. (b) SEM/EDS elemental map of phosphorous (blue) of the same area, showing high phosphorous content in veins extending from the tip of the crack.

Figure 6: Microhardness traverse across the 17 mm/s weld in the as polished condition. (a) Micrograph showing hardness indents and the centerline solidification crack. (b) Microhardness traverse that shows that the fusion zone is approximately twice as hard as the base metal and heat affected zone.

Figure 7: Micrographs of the 17 mm/s weld in the etched condition showing martensite formation. (a) near the fusion line with the HAZ on the right side of the micrograph, and (b) in the fusion zone next to a large cohenite band on the left side of the micrograph.

(a)

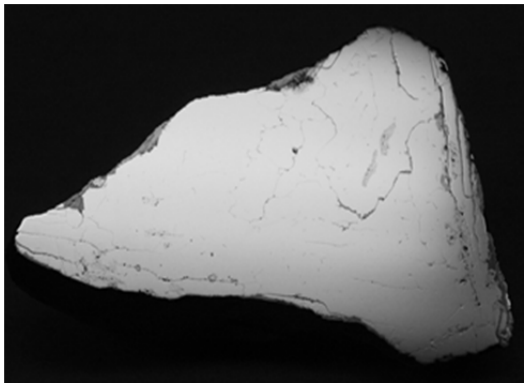

(b)

Figure 1

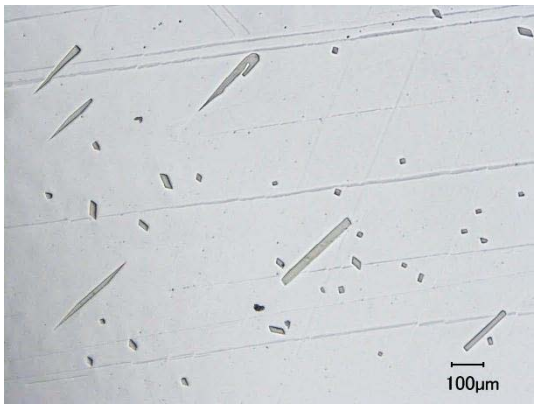

(a)

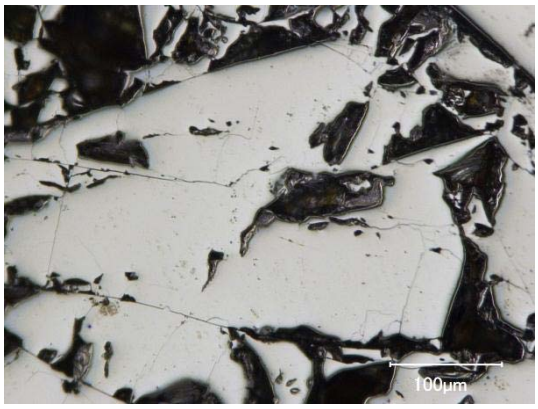

(b)

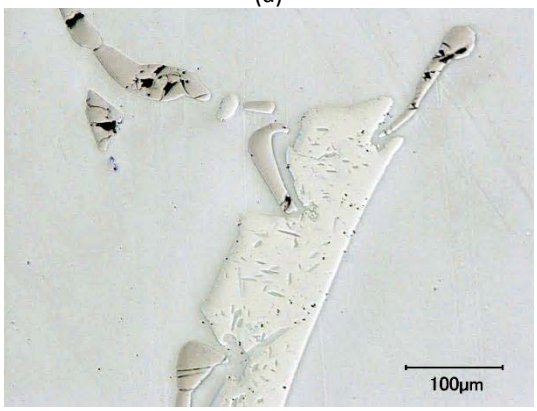

(c)

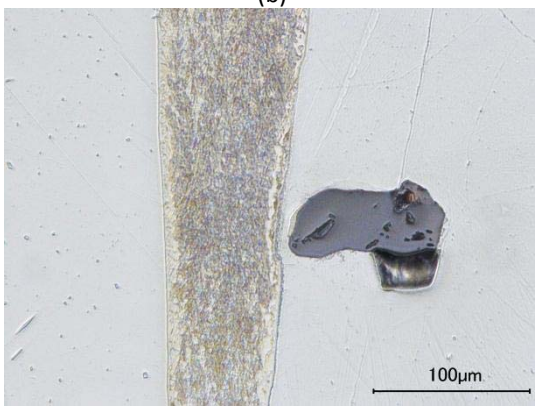

(d)

Figure 2

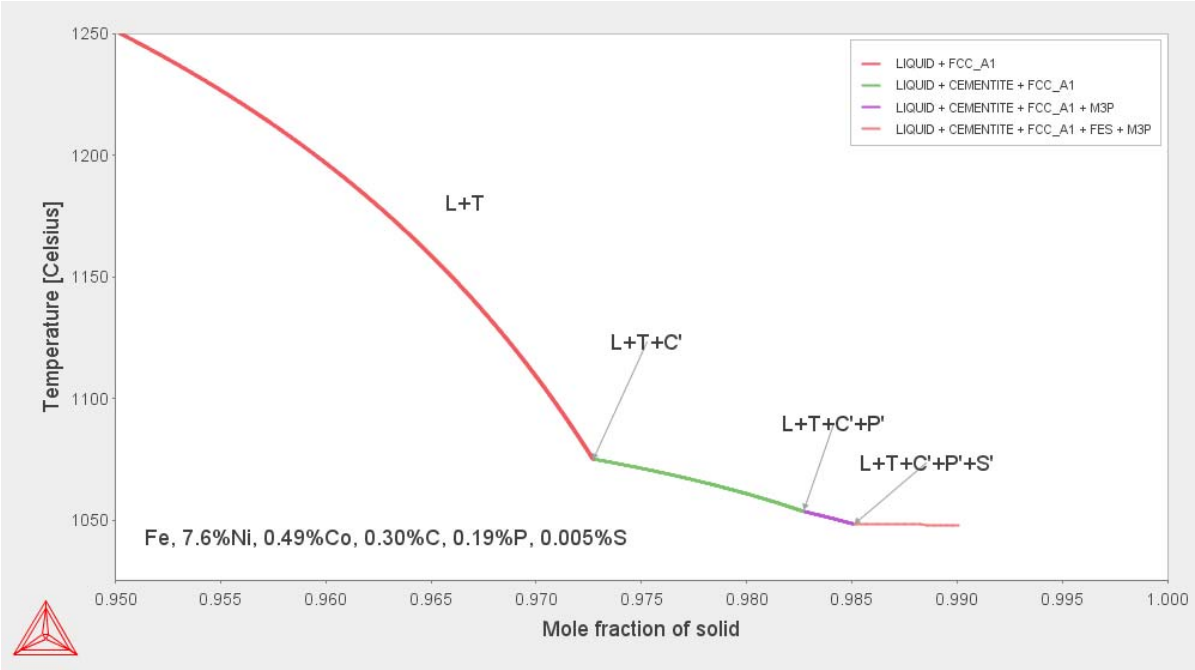

Figure 3

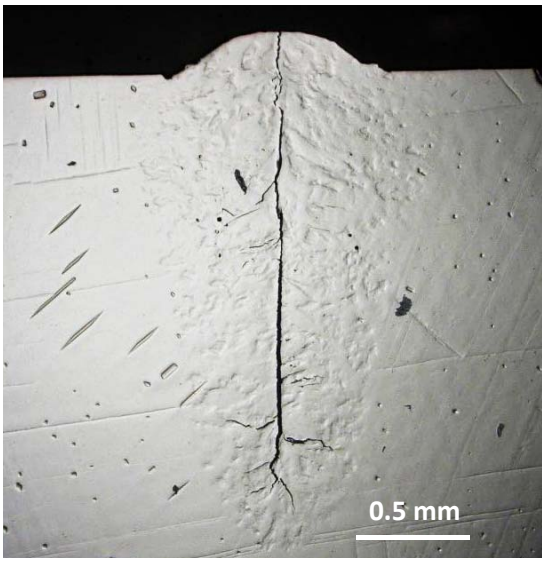

(a)

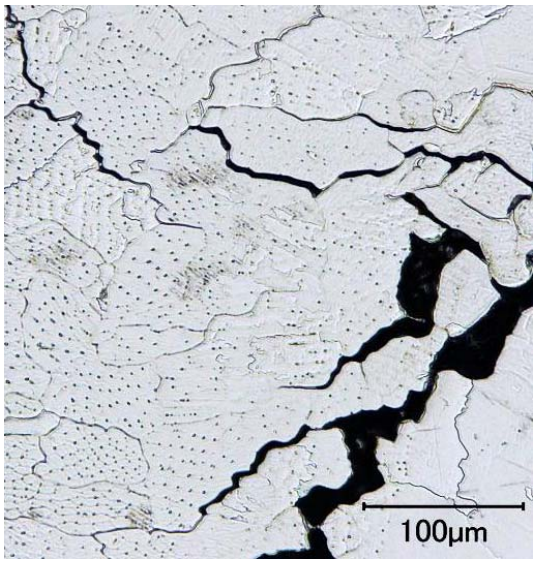

(b)

Figure 4

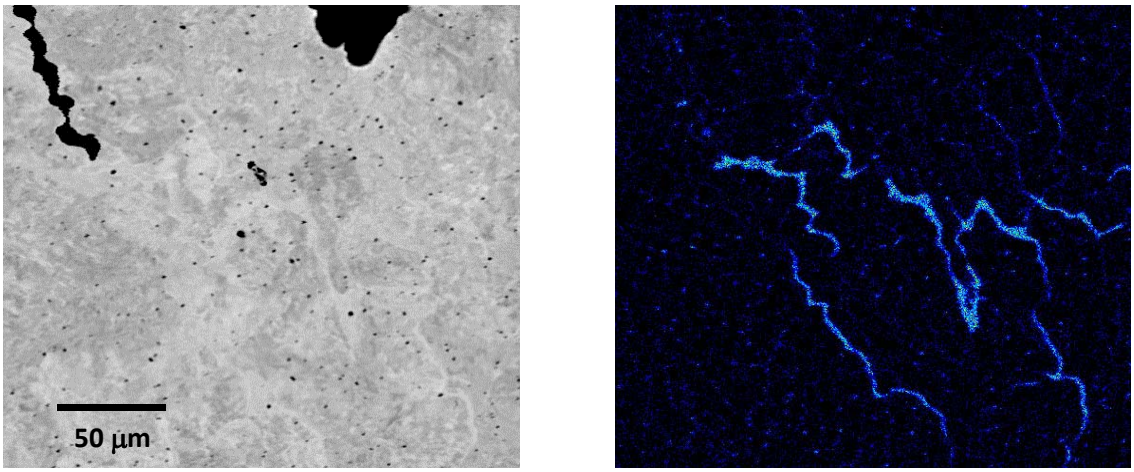

(a) (b)

Figure 5

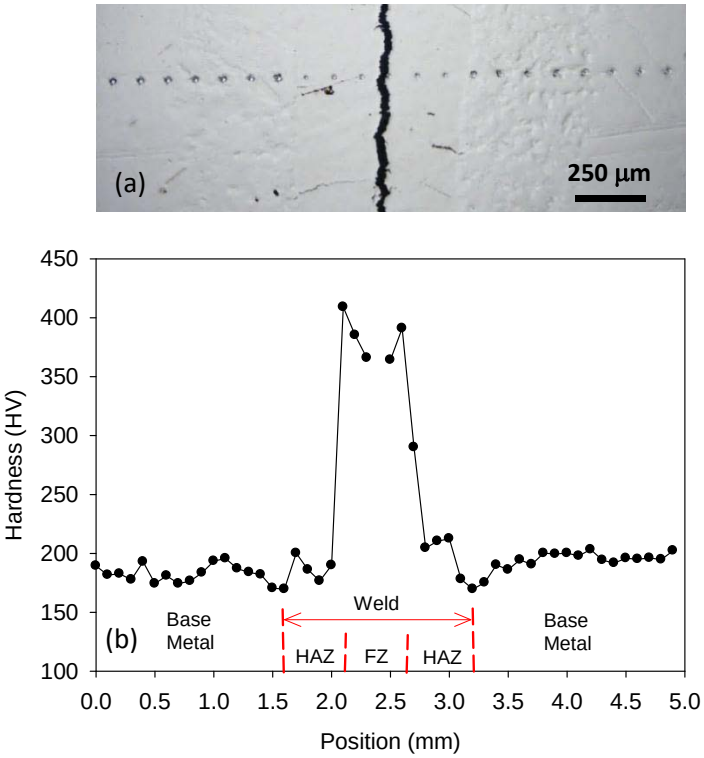

Figure 6

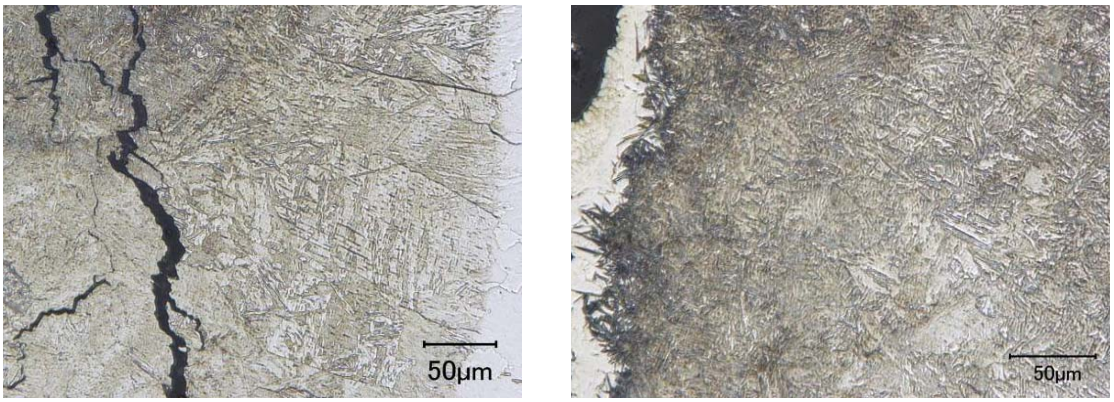

(a) (b)

Figure 7